SI-UAS 2016 manuscript No.
(will be inserted by the editor)

Nonlinear Control With Swing Damping of a Multirotor UAV with Suspended Load

Kristian Klausen · Thor I. Fossen · Tor Arne Johansen

Received: date / Accepted: date

Abstract In this paper, we consider the problem of trajectory tracking of a multirotor Unmanned Aerial Vehicle carrying a suspended payload. The movement of the suspended payload influences the dynamics of the multirotor, which must be appropriately handled by the controller to achieve satisfactory tracking results. We derive a mathematical model of the interconnected multi-body system using Kane's equations, and develop a non-linear tracking controller based on the backstepping technique. In addition to suppressing the effects of the swinging payload, the controller also compensates for an unknown constant wind disturbance. The origin of the tracking error is proven UGAS (Uniformly Globally Asymptotically Stable) and ULES (Uniformly Locally Exponentially Stable) through Lyapunov analysis. To reduce the swing motion of the suspended load, a nominal swing-free path is generated through open loop shaping filters, then further perturbed through a delayed feedback approach from measured load deflection angles to achieve robustness.

The proposed controller structure is verified by simulations and experiments.

Keywords Unmanned Aerial Vehicles · Non-linear control · Modeling

1 Introduction

Unmanned Aerial Vehicles (UAVs) have seen a rise in public awareness in the past years. Although UAV research is a field of long and rich history, the availability of cheap sensors and computing power have seen a new generation of UAVs available at a fraction of the cost. Where civilian applications were previously driven by hobbyists and enthusiasts, new technology now enables several new product opportunities. Aerial surveillance is an obvious example, where autonomous vehicles can be used to survey locations on a regular basis.

UAVs can also intervene with the environment in the form of pickup, placement and transportation of objects. These objects could be sensors [6], or delivery of packages to consumers [2]. The ability for aircrafts, specifically Vertical Takeoff and Landing Vehicles (VTOL), to carry an object suspended by a wire has been much studied, ranging from military applications were a pilot manually transported supplies, to comprehensive studies on the dynamics of coordinated lifting operations [9]. Recently, smaller multirotor UAVs have been used for such tasks. In [20], the authors study it's dynamics and present an adaptive scheme and derives a path-planning algorithm that minimizes the load swing. Highly agile movements with one or more such UAVs is studied in [14].

In this paper, we consider a multirotor UAV charged with the task of transporting a suspended payload. In our earlier work [17], we developed a non-linear tracking controller for the UAV, and provided validation by numerical simulations. This paper expands that work by adding robustness to the controller in the case of wind, and experimental validation. After an initial overview of the problem in Section 2, the dynamics of the multirotor-load system is derived in Section 3 using Kane's equations [10]. In Section 4, a non-linear backstepping controller *with integral action* is proposed, followed by stability proofs using Lyapunov theory. The controller is then verified by numerical simulations and experimental tests. *This is the main contribution in this work.*

K. Klausen · T. I. Fossen · T. A. Johansen
Norwegian University of Science and Technology
Department of Engineering Cybernetics
E-mail: kristian.klausen@itk.ntnu.no

Methods from the literature for suspended load swing angle control is discussed in Section 6, followed by a second case-study of numerical simulations and experiments. The paper is concluded in Section 8.

2 Problem Description and Control Strategies

We consider the objective of the UAV to safely transport a suspended payload, by tracking a user defined trajectory or waypoint route, while suppressing the disturbance from the load swing and external environmental effects, such as wind. The UAV in question is equipped with an internal Inertial Measurement Unit (IMU) and GNSS[1] system, with the accompanied navigation filter providing full state (attitude and position) output for the controllers. Further, the attachment-point of the suspended load is a gimbal-like structure, providing measurements of the displacement angles (relative to the UAV body) of the load suspended by a wire, as seen in Figure 1.

For control, there are two aspects that needs to be addressed.

(i) Tracking control of the UAV, while suppressing effects from the swinging suspended mass and environmental forces.
(ii) Reducing the swing motion of the suspended load.

Model-based techniques to cancel the effect of the load, for objective (i), are popular in the literature. [21] considers the effect of the swinging payload as a change in CoG of the vehicle, and employs an adaptive scheme to compensate for the motion. On the other hand, in [5], the tension of the suspended payload is used as feedforward to cancel the effects on a small-scale helicopter. The latter, objective (ii), can be a part of the control objective for the vehicle as demonstrated in [15], as an extra feedback to manipulate the reference trajectory [8], or as part of the trajectory planning phase [7].

In this work, we will utilize a backstepping type controller [18] to create stabilizing shaping functions to achieve a robust tracking controller to solve objective (i). The results from [8], combined with well known open-loop trajectory generation tools, will be utilized to robustly solve objective (ii).

[1] Global Navigation Satellite Systems

Fig. 1 Hexacopter type multirotor carrying a suspended load. The mechanism under the UAV body provides measurements of the deflection angle of the attachment wire.

3 Modeling

The dynamic modeling of a multirotor type UAV is well studied in the literature. For a detailed survey, see [19] and references therein. Different choices of kinematic representation of attitude are made throughout the literature. Euler angles are popular and common, and forms the basis for linearized PID control around the hover-state. This is the controller-type found in many commercial autopilots, due to it's simplicity and strong connection to the terms commonly used in fixed-wing avionics. The inherent downside of this representation is a representation singularity, typically when the pitch angle is $\pm 90°$. This is, however, outside the operating range of the UAV in this paper.

Let $\{n\}$ be the frame whos axes points in North, East and Down (NED) direction, which is assumed inertial. The multirotor position in $\{n\}$ is given by $\mathbf{p} \in \mathbb{R}^3$. Further, let $\{b\}$ be a body-fixed coordinate system. Its orientation with respect to $\{n\}$ is given by three consecutive rotations about the axis z, y, and x, respectively. This corresponds to the Euler zyx representation [12].

$$\dot{\mathbf{p}} = \mathbf{v} \tag{1}$$

$$\dot{\boldsymbol{\Theta}} = \mathbf{T}(\boldsymbol{\Theta})\boldsymbol{\omega} \tag{2}$$

where $\boldsymbol{\Theta} := [\phi, \theta, \psi]^{\mathrm{T}}$ is a vector of the roll, pitch and yaw angles, $\boldsymbol{\omega}$ is the angular body velocity, and $\mathbf{T}(\boldsymbol{\Theta})$ is

$$\mathbf{T}(\boldsymbol{\Theta}) := \begin{bmatrix} 1 & \sin\phi\,\tan\theta & \cos\phi\,\tan\theta \\ 0 & \cos\phi & -\sin\phi \\ 0 & \frac{\sin\phi}{\cos\theta} & \frac{\cos\phi}{\cos\theta} \end{bmatrix}, \cos(\theta) \neq 0 \tag{3}$$

The dynamics can be derived by classical Newtonian or Lagrangian methods, and readers are referred to [19] for details on its derivation.

$$\dot{\mathbf{p}} = \mathbf{v} \tag{4}$$
$$m_c\dot{\mathbf{v}} = m_c\mathbf{g} + \mathbf{R}(\boldsymbol{\Theta})f + \mathbf{w} \tag{5}$$
$$\dot{\boldsymbol{\Theta}} = \mathbf{T}(\boldsymbol{\Theta})\boldsymbol{\omega} \tag{6}$$
$$I\dot{\boldsymbol{\omega}} = \mathbf{S}(I\boldsymbol{\omega})\boldsymbol{\omega} + \mathbf{M} \tag{7}$$

where $\mathbf{p} \in \mathbb{R}^3$ is the UAV position in the inertial frame $\{n\}$, $\mathbf{v} \in \mathbb{R}^3$ the linear velocity in $\{n\}$, $\mathbf{R}(\boldsymbol{\Theta}) \in \mathcal{SO}^3$ a rotation matrix from the inertial frame $\{n\}$ to the body-fixed frame $\{b\}$, $\boldsymbol{\omega} \in \mathbb{R}^3$ the angular velocity of the UAV, represented in $\{b\}$. Further, the operator $\mathbf{S}(\cdot)$ is the skew-symmetric transformation, such that $p \times q = \mathbf{S}(p)q$. m_c is the mass of the UAV, and I the body-fixed inertia matrix. f is vertical thrust directed along the negative body-aligned z-axis, and $\mathbf{M}$ are applied torque about the UAV from the motors. $\mathbf{w}$ is additional environmental forces, such as wind disturbance and finally $\mathbf{g} = \begin{bmatrix}0 & 0 & g\end{bmatrix}^{\mathrm{T}}$, where g is the gravitational constant.

Consider now a load being suspended in the centre of gravity of the UAV. This will affect the translational motion (5) by a term $\boldsymbol{\tau}_L$, parameterized by the load dynamics, but the rotational motion (7) is unaffected. As control of the attitude of the multirotor is not the task of the trajectory tracking controller, the model describing the translational motion is now

$$\dot{\mathbf{p}} = \mathbf{v} \tag{8}$$
$$m_c\dot{\mathbf{v}} = m_c\mathbf{g} + \mathbf{R}(\boldsymbol{\Theta})f + \boldsymbol{\tau}_L + \mathbf{w} \tag{9}$$

Further, assume now that a sufficiently fast attitude controller is present. The direction of the applied force for translational motion is given by $\mathbf{R}$, and by manipulating the roll and pitch angles of the UAV we can apply force in a desired direction. An example of such a controller is given in [19], and directly for Euler angles in Appendix A. Thus, the term $\mathbf{R}(\boldsymbol{\Theta})f$ can be replaced by an inertial control force $\mathbf{F} = \mathbf{R}(\boldsymbol{\Theta})f \in \mathbb{R}^3$, resulting in

$$\dot{\mathbf{p}} = \mathbf{v} \tag{10}$$
$$m_c\dot{\mathbf{v}} = m_c\mathbf{g} + \mathbf{F} + \boldsymbol{\tau}_L + \mathbf{w} \tag{11}$$

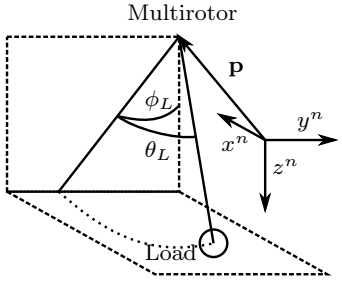

Fig. 2 Illustration of pendulum angle parameterization by two consecutive rotations ϕ_L and θ_L about the x- and y-axis, respectively.

Next, the suspended load dynamics is modeled as a pendulum. This simple model has been used with success in earlier work [6]. We consider the suspended load as a point-mass, connected by a rigid link to the CoG of the UAV. This is valid for non-aggressive maneuvers where the wire remains taut. We parameterize the pendulum displacements by ϕ_L and θ_L, which are the load rotation angles about the inertial x- and y-axis, respectively, see Figure 2. The generalized coordinates for the system are thus $\boldsymbol{\eta} = [\mathbf{p}^{\mathrm{T}}, \phi_L, \theta_L]^{\mathrm{T}}$. Physical damping of the pendulum swing is modeled by a linear damping term, which is valid for low speeds. By utilizing Kane's equation [10], we get the dynamical model (12):

$$\begin{aligned} \dot{\boldsymbol{\eta}} &= \boldsymbol{\nu} \\ \mathbf{M}^*(\boldsymbol{\eta})\dot{\boldsymbol{\nu}} + \mathbf{C}^*(\boldsymbol{\eta},\boldsymbol{\nu})\boldsymbol{\nu} + \mathbf{G}(\boldsymbol{\eta}) + \mathbf{D}\boldsymbol{\nu} &= \boldsymbol{\tau} + \boldsymbol{\tau}_a \end{aligned} \tag{12}$$

where $\mathbf{M}^*(\boldsymbol{\eta})$ and $\mathbf{C}^*(\boldsymbol{\eta},\boldsymbol{\nu})$ can be seen in (13)–(14), $\boldsymbol{\tau} := \begin{bmatrix}\mathbf{F}^{\mathrm{T}} & \mathbf{0}_{1\times 2}\end{bmatrix}^{\mathrm{T}}$, $\boldsymbol{\nu} := [\mathbf{v}^{\mathrm{T}}, \dot{\phi}_L, \dot{\theta}_L]^{\mathrm{T}}$, $\boldsymbol{\tau}_a := \begin{bmatrix}\mathbf{w}^{\mathrm{T}} & \mathbf{0}_{1\times 2}\end{bmatrix}^{\mathrm{T}}$ and

$$\mathbf{G}(\boldsymbol{\eta}) = \begin{bmatrix} 0 \\ 0 \\ -g\ (m_L + m_c) \\ L\,g\,m_L\,\cos\theta_L\,\sin\phi_L \\ L\,g\,m_L\,\cos\phi_L\,\sin\theta_L \end{bmatrix}. \tag{15}$$

The term $\mathbf{D}\boldsymbol{\nu}$ is the linear damping force, incorporating the effects of air drag at low speed. $\mathbf{D} = \mathtt{diag}\{[0,0,0,d,d]\}$, where $d > 0$ is a drag coefficient. $\mathbf{w}$ is an unknown disturbance acting on the body of the UAV, typically wind. This is assumed constant, or slowly varying.

As can be seen in (12), the equations are organized in matrix form, which is typical in the literature of robotic manipulation. This form greatly simplifies the control analysis. In fact, as is common in robotic manipulators, the matrix $\dot{\mathbf{M}}^*(\boldsymbol{\eta}) - 2\mathbf{C}^*(\boldsymbol{\eta},\boldsymbol{\nu})$ is skew symmetric, which is a very useful property in Lyapunov

$$\mathbf{M}^*(\boldsymbol{\eta}) = \begin{bmatrix} m_L + m_c & 0 & 0 & 0 & L\,m_L\,\mathrm{c}\theta_L \\ 0 & m_L + m_c & 0 & -L\,m_L\,\mathrm{c}\phi_L\,\mathrm{c}\theta_L & L\,m_L\,\mathrm{s}\phi_L\,\mathrm{s}\theta_L \\ 0 & 0 & m_L + m_c & -L\,m_L\,\mathrm{c}\theta_L\,\mathrm{s}\phi_L & -L\,m_L\,\mathrm{c}\phi_L\,\mathrm{s}\theta_L \\ 0 & -L\,m_L\,\mathrm{c}\phi_L\,\mathrm{c}\theta_L & -L\,m_L\,\mathrm{c}\theta_L\,\mathrm{s}\phi_L & L^2\,m_L\,\mathrm{c}\theta_L{}^2 & 0 \\ L\,m_L\,\mathrm{c}\theta_L & L\,m_L\,\mathrm{s}\phi_L\,\mathrm{s}\theta_L & -L\,m_L\,\mathrm{c}\phi_L\,\mathrm{s}\theta_L & 0 & L^2\,m_L \end{bmatrix} \tag{13}$$

$$\mathbf{C}^*(\boldsymbol{\eta},\boldsymbol{\nu}) = \begin{bmatrix} 0\,0\,0 & 0 & -L\,\dot{\theta}_L\,m_L\,\mathrm{s}\theta_L \\ 0\,0\,0 & L\,m_L\left(\dot{\phi}_L\,\mathrm{c}\theta_L\,\mathrm{s}\phi_L + \dot{\theta}_L\,\mathrm{c}\phi_L\,\mathrm{s}\theta_L\right) & L\,m_L\left(\dot{\phi}_L\,\mathrm{c}\phi_L\,\mathrm{s}\theta_L + \dot{\theta}_L\,\mathrm{c}\theta_L\,\mathrm{s}\phi_L\right) \\ 0\,0\,0 & -L\,m_L\left(\dot{\phi}_L\,\mathrm{c}\phi_L\,\mathrm{c}\theta_L - \dot{\theta}_L\,\mathrm{s}\phi_L\,\mathrm{s}\theta_L\right) & -L\,m_L\left(\dot{\theta}_L\,\mathrm{c}\phi_L\,\mathrm{c}\theta_L - \dot{\phi}_L\,\mathrm{s}\phi_L\,\mathrm{s}\theta_L\right) \\ 0\,0\,0 & -\frac{1}{2}L^2\,\dot{\theta}_L\,m_L\,\mathrm{s}(2\,\theta_L) & -\frac{1}{2}L^2\,\dot{\phi}_L\,m_L\,\mathrm{s}(2\,\theta_L) \\ 0\,0\,0 & \frac{1}{2}L^2\,\dot{\phi}_L\,m_L\,\mathrm{s}(2\,\theta_L) & 0 \end{bmatrix} \tag{14}$$

analysis. As can be seen from (13), $\mathbf{M}^*(\boldsymbol{\eta})$ is singular at $\theta_L = \pi/2$. This is due to the representation of the pendulum configuration, and it corresponds to the case where the suspended load is directed out of the nose of the UAV. Although while in this configuration the rigid-link assumption is unlikely to hold in practice, and would most likely result in a crash due to impact between the suspended load and multirotor propellers, this situation is prevented by the design of the controller. We illustrate in the next section how a infinitesimal *singularity avoidance* term can be added to use the model for theoretically valid control design and analysis.

4 Control design

In this section, we design a nonlinear trajectory-tracking controller for the UAV, to resolve objective (i). We utilize the backstepping technique [18], to design the controllers in two steps. To achieve this, with a slight abuse of terminology, we view (12) as an underactuated system, in which elements 4 and 5 of the control input vector $\boldsymbol{\tau}$ are constrained to be zero. The design procedure is inspired by [11].

The model developed in the previous section has a representation singularity at $\theta_L = \pi/2$. This is an undesired feature when designing the control system. Thus, we create a perturbed model, in which we avoid the singularity by adding an infinitesimal *singularity avoidance* term at $\mathbf{M}^*_{4,4}$. The model used for control design are then:

$$\dot{\boldsymbol{\eta}} = \boldsymbol{\nu} \tag{16}$$

$$\mathbf{M}(\boldsymbol{\eta})\dot{\boldsymbol{\nu}} + \mathbf{C}(\boldsymbol{\eta},\boldsymbol{\nu})\boldsymbol{\nu} + \mathbf{G}(\boldsymbol{\eta}) + \mathbf{D}\boldsymbol{\nu} = \boldsymbol{\tau} + \boldsymbol{\tau}_a \tag{17}$$

where $\mathbf{M}(\boldsymbol{\eta}) = \mathbf{M}^*(\boldsymbol{\eta})$, $\mathbf{C}(\boldsymbol{\eta},\boldsymbol{\nu}) = \mathbf{C}^*(\boldsymbol{\eta},\boldsymbol{\nu})$ except for

$$\mathbf{M}(\boldsymbol{\eta})_{4,4} = L^2 m_L \cos\theta_L{}^2 + \varepsilon \sin\theta_L{}^2, \tag{18}$$

and

$$\mathbf{C}(\boldsymbol{\eta},\boldsymbol{\nu})_{4,4} = -\frac{1}{2}L^2 m_L \dot{\theta}_L \sin 2\theta_L + \frac{1}{2}\varepsilon\dot{\theta}_L \sin 2\theta_L. \tag{19}$$

$\varepsilon > 0$ is a small positive constant. As can be seen, $\mathbf{C}(\boldsymbol{\eta},\boldsymbol{\nu})$ is also perturbed to maintain the skew-symetric property. This added term ensures that the mass matrix is non-singular for all $(\theta_L,\, \phi_L)$ and close to the original model for small $(\theta_L,\, \phi_L)$. This perturbed model is now used in the rest of this section.

Consider now a sufficiently smooth desired trajectory $\mathbf{r}(t)$. We define the error signals $\mathbf{z}_1 \in \mathbb{R}^3$ and $\mathbf{z}_2 \in \mathbb{R}^5$ as

$$\mathbf{z}_1 := \mathbf{p} - \mathbf{r} \tag{20}$$

$$\mathbf{z}_2 := [z_{2,1}, z_{2,2}, z_{2,3}, z_{2,4}, z_{2,5}]^{\mathrm{T}} := \boldsymbol{\nu} - \boldsymbol{\alpha} \tag{21}$$

where $\boldsymbol{\alpha} := [\alpha_1, \alpha_2, \alpha_3, \alpha_4, \alpha_5]^{\mathrm{T}} \in \mathbb{R}^5$ is a vector of stabilizing functions to be specified later.

Now, we utilize a selection matrix $\mathbf{H}$ to select the states of $\mathbf{z}_1$ we are interested in for control. Let

$$\mathbf{H} = \begin{bmatrix} 1\,0\,0\,0\,0 \\ 0\,1\,0\,0\,0 \\ 0\,0\,1\,0\,0 \end{bmatrix} \tag{22}$$

such that the error-dynamics becomes

$$\dot{\mathbf{z}}_1 = \mathbf{H}\boldsymbol{\nu} - \dot{\mathbf{r}} \tag{23}$$

and

$$\begin{aligned} \mathbf{M}(\boldsymbol{\eta})\dot{\mathbf{z}}_2 &= \mathbf{M}(\boldsymbol{\eta})\dot{\boldsymbol{\nu}} - \mathbf{M}(\boldsymbol{\eta})\dot{\boldsymbol{\alpha}} \\ &= \boldsymbol{\tau} + \tau_a - \mathbf{C}(\boldsymbol{\eta},\boldsymbol{\nu})\boldsymbol{\nu} - \mathbf{G}(\boldsymbol{\eta}) \\ &\quad - \mathbf{D}\boldsymbol{\nu} - \mathbf{M}(\boldsymbol{\eta})\dot{\boldsymbol{\alpha}} \end{aligned} \tag{24}$$

4.1 Step 1

Consider a Lyapunov function candidate (LFC) for the first sub-system (23) as

$$V_1(\mathbf{z}_1, t) = \frac{1}{2}\mathbf{z}_1^{\mathrm{T}}\mathbf{z}_1 \tag{25}$$

It's derivative along the solution of $\mathbf{z}_1(t)$ is

$$\begin{aligned}\dot{V}_1(\mathbf{z}_1, t) &= \mathbf{z}_1^{\mathrm{T}}(\mathbf{H}\boldsymbol{\nu} - \dot{\mathbf{r}}) \\ &= \mathbf{z}_1^{\mathrm{T}}(\boldsymbol{\alpha}_{1:3} + \mathbf{H}\mathbf{z}_2 - \dot{\mathbf{r}})\end{aligned} \tag{26}$$

where $(\cdot)_{i:j}$ represents elements i to j of the vector $(\cdot)$. By designing the stabilizing functions $\boldsymbol{\alpha}_{1:3}$ as

$$\boldsymbol{\alpha}_{1:3} = \dot{\mathbf{r}} - \mathbf{K}_1\mathbf{z}_1, \tag{27}$$

where $\mathbf{K}_1 = \mathbf{K}_1^{\mathrm{T}} > 0$ is a positive definite matrix. The derivative of $V_1(\mathbf{z}_1, t)$ becomes

$$\dot{V}_1(\mathbf{z}_1, t) = -\mathbf{z}_1^{\mathrm{T}}\mathbf{K}_1\mathbf{z}_1 + \mathbf{z}_1^{\mathrm{T}}\mathbf{H}\mathbf{z}_2 \tag{28}$$

4.2 Step 2

Take the second LFC as

$$V_2(\mathbf{z}_1, \mathbf{z}_2, \boldsymbol{\xi}, t) = V_1(\mathbf{z}_1, t) + \frac{1}{2}\mathbf{z}_2^{\mathrm{T}}\mathbf{M}(\boldsymbol{\eta})\mathbf{z}_2 \tag{29}$$

which is positive definite for $(\mathbf{z}_1, \mathbf{z}_2) \neq 0$. Taking the derivative of (29) yields:

$$\begin{aligned}\dot{V}_2(\mathbf{z}_1, \mathbf{z}_2, t) &= -\mathbf{z}_1^{\mathrm{T}}\mathbf{K}_1\mathbf{z}_1 \\ &\quad + \mathbf{z}_2^{\mathrm{T}}(\boldsymbol{\tau} + \boldsymbol{\tau}_a - \mathbf{C}\boldsymbol{\alpha} - \mathbf{G} - \mathbf{D}\boldsymbol{\nu} + \mathbf{H}^{\mathrm{T}}\mathbf{z}_1 - \mathbf{M}\dot{\boldsymbol{\alpha}})\end{aligned}$$

where we have utilized the skew-symetric property of $\frac{1}{2}\dot{\mathbf{M}}(\boldsymbol{\eta}) - \mathbf{C}(\boldsymbol{\eta}, \boldsymbol{\nu})$. Suppose now that the control $\boldsymbol{\tau}$ can be set to

$$\boldsymbol{\tau} = \mathbf{C}\boldsymbol{\alpha} + \mathbf{G} + \mathbf{D}\boldsymbol{\alpha} - \mathbf{H}^{\mathrm{T}}\mathbf{z}_1 + \mathbf{M}\dot{\boldsymbol{\alpha}} - \mathbf{K}_2\mathbf{z}_2 \tag{30}$$

where $\mathbf{K}_2 = \mathbf{K}_2^{\mathrm{T}} > 0$. By remembering $\boldsymbol{\tau}_a = \mathbf{H}^{\mathrm{T}}\mathbf{w}$, this results in

$$\dot{V}_2(\mathbf{z}_1, \mathbf{z}_2, t) = -\mathbf{z}_1^{\mathrm{T}}\mathbf{K}_1\mathbf{z}_1 - \mathbf{z}_2^{\mathrm{T}}\mathbf{K}_2\mathbf{z}_2 - \mathbf{z}_2^{\mathrm{T}}\mathbf{D}\mathbf{z}_2 + \mathbf{z}_2^{\mathrm{T}}\mathbf{H}^{\mathrm{T}}\mathbf{w}$$

Clearly, if $\mathbf{w} \equiv 0$, or if it was exactly known, it could be cancelled by the controller. Since this is quite unrealistic, we use the augmented controller

$$\boldsymbol{\tau} = \mathbf{C}\boldsymbol{\alpha} + \mathbf{G} + \mathbf{D}\boldsymbol{\alpha} - \mathbf{H}^{\mathrm{T}}\mathbf{z}_1 + \mathbf{M}\dot{\boldsymbol{\alpha}} - \mathbf{K}_2\mathbf{z}_2 - \mathbf{H}^{\mathrm{T}}\hat{\mathbf{w}} \tag{31}$$

where $\hat{\mathbf{w}}$ is the estimate of $\mathbf{w}$, given by

$$\dot{\hat{\mathbf{w}}} = \rho\mathbf{H}\mathbf{z}_2 \tag{32}$$

where $\rho \in \mathbb{R}$ is a tuning parameter.

In the following lemma, we show that with this choice of $\boldsymbol{\tau}$ and update law for $\hat{\mathbf{w}}$, the origin of the system (23)–(24) and (32) is *Uniformly Globally Asymptotically Stable* (UGAS) and *Uniformly Locally Exponentially Stable* (ULES). However, as we cannot set a desired moment about the suspension point of the load, the fourth and fifth row of (31) must instead be equal to zero. In Section 4.3, we design the remaining stabilizing functions to achieve this.
The closed-loop system can be written as

$$\begin{bmatrix}\dot{\mathbf{z}}_1 \\ \dot{\mathbf{z}}_2\end{bmatrix} = \begin{bmatrix}-\mathbf{K}_1 & \mathbf{H} \\ A_{21}(t) & A_{22}(t)\end{bmatrix}\begin{bmatrix}\mathbf{z}_1 \\ \mathbf{z}_2\end{bmatrix} + \begin{bmatrix}0 \\ \mathbf{M}^{-1}(\Theta(t))\mathbf{H}^{\mathrm{T}}\end{bmatrix}\tilde{\mathbf{w}} \tag{33}$$

$$\dot{\tilde{\mathbf{w}}} = \rho\mathbf{H}\mathbf{z}_2 \tag{34}$$

where

$$\begin{aligned}A_{21}(t) &:= -\mathbf{M}^{-1}(\Theta(t))\mathbf{H}^{\mathrm{T}} \\ A_{22}(t) &:= \mathbf{M}^{-1}(\Theta(t))(-\mathbf{K}_2 - \mathbf{D} - \mathbf{C}(\Theta(t), \dot{\Theta}(t)))\end{aligned}$$

and $\Theta(t) := [\theta_L(t), \phi_L(t)]^{\mathrm{T}}$.

Lemma 1 *The origin of* (33)–(34) *is UGAS and ULES.*

Proof To prove UGAS and ULES of the equilibrium point $(\mathbf{z}_1, \mathbf{z}_2, \tilde{w}) = 0$ of (33)–(34), we apply the results from [13]. To this end, the closed-loop system (33)–(34) can be restated in the form:

$$\dot{x}_1 = h(x_1, t) + G(x, t)x_2 \tag{35}$$

$$\dot{x}_2 = -PG(x, t)^{\mathrm{T}}\left(\frac{\partial W(x_1, t)}{\partial x_1}\right)^{\mathrm{T}},\ P = P^{\mathrm{T}} > 0 \tag{36}$$

where

$$\begin{aligned}x_1 &:= \begin{bmatrix}\mathbf{z}_1 & \mathbf{z}_2\end{bmatrix}^{\mathrm{T}} \\ x_2 &:= \tilde{\mathbf{w}} \\ h(x_1, t) &:= \begin{bmatrix}-\mathbf{K}_1 & \mathbf{H} \\ A_{21}(t) & A_{22}(t)\end{bmatrix}x_1 \\ G(x, t) &:= \begin{bmatrix}0 & \mathbf{M}^{-1}(\Theta(t))\mathbf{H}^{\mathrm{T}}\end{bmatrix}^{\mathrm{T}} \\ P &:= \rho\mathbf{I} \\ W(x_1, t) &= \frac{1}{2}\mathbf{z}_2^{\mathrm{T}}\mathbf{M}\mathbf{z}_2 + \frac{1}{2}\mathbf{z}_1^{\mathrm{T}}\mathbf{z}_1 \\ &\Rightarrow \frac{\partial W(x_1, t)}{\partial x_1} = \begin{bmatrix}\mathbf{z}_1 & \mathbf{M}(\Theta(t))\mathbf{z}_2\end{bmatrix}\end{aligned}$$

[13, Theorem 1] states that if the conditions (A1)–(A2) below hold, the origin of the system (35)–(36) is UGAS and ULES. Let $G_0(x_2, t) := G(x, t)|_{x_1 \equiv 0}$, and $\rho_j : \mathbb{R}_{\geq 0} \to \mathbb{R}_{\geq 0}$, $(j = 1, 2, 3)$ be continuous nondecreasing functions. The conditions of A1 are

$$\max\left\{\|h(x_1,t)\|, \left\|\frac{\partial W(x_1,t)}{\partial x_1}\right\|\right\} \leq \rho_1(||x_1||)||x_1|| \tag{A1.a}$$

$$\max\left\{\|G(x,t)\|, \|G_0(x_2,t)\|\right\} \leq \rho_2(||x||) \tag{A1.b}$$

$$\max\left\{\left\|\frac{\partial G_0(x_2,t)}{\partial x_2}\right\|, \left\|\frac{\partial G_0(x_2,t)}{\partial t}\right\|\right\} \leq \rho_3(||x_2||) \tag{A1.c}$$

Indeed, (A1.a) holds because $\mathbf{M}(\Theta(t))$ is non-singular, and is bounded for all $\Theta(t)$. Further, as we have $G_0(x_2,t) = \left[0\ \mathbf{M}^{-1}(\Theta(t))\mathbf{H}^{\mathrm{T}}\right]^{\mathrm{T}}$, (A1.b) holds since $\mathbf{M}(\Theta(t))$ has an upper bound. In fact, there exists $m_m, m_M \in \mathbb{R}$ s.t. $\mathbf{I}m_m \leq \mathbf{M}(\Theta(t)) \leq \mathbf{I}m_M$.

By noting that the system (35)–(36) is *forward complete* [3], we have existence and boundedness of $\dot{\Theta}\ \forall t$. Thus, the partial time derivative of $G_0(x_2,t)$ is bounded, and (A1.c) holds. Additionally, we need the condition

$$G_0(x_2,t)^{\mathrm{T}} G_0(x_2,t) \geq b_m \mathbf{I} \tag{A1.d}$$

which holds with in our case with $b_m = (1/m_M^2)\mathbf{I}$

Further, let κ_1, κ_2 be class-$\mathcal{K}_\infty$ functions, and $c > 0$ a strictly positive real number. Then, we need

$$\kappa_1(\|x_1\|) \leq W(x_1,t) \leq \kappa_2(\|x_1\|) \tag{A2.a}$$

$$\frac{\partial W(x_1,t)}{\partial t} + \frac{\partial W(x_1,t)}{\partial x_1} h(x_1,t) \leq -c\|x_1\|^2 \tag{A2.b}$$

Clearly, by setting $\kappa_1 = 0.5k_1\|x_1\|^2$, $\kappa_2 = 0.5k_2\|x_1\|^2$ where $k_1 = \min(m_m, 1), k_2 = \max(m_M, 1)$, (A2.a) holds. (A2.b) expands to

$$-\mathbf{z}_1^{\mathrm{T}}\mathbf{K}_1\mathbf{z}_1 - \mathbf{z}_2^{\mathrm{T}}\mathbf{K}_2\mathbf{z}_2 \leq -c\|x_1\|^2 \tag{37}$$

with $c = \min\{\inf(\mathbf{K}_1), \inf(\mathbf{K}_2)\}$. In addition, we have $\kappa_2(s) \propto s^2$.

We have now shown that all the assumptions (A1-A2) of [13, Theorem 1] holds, and conclude that the origin of(35)–(36) is UGAS and ULES. □

4.3 Remaining stabilizing functions

We now design the remaining stabilizing functions α_4 and α_5 to ensure that the fourth and fifth row of (31) is indeed zero. By extracting these rows from (31), we get the constraint equations

$$\boldsymbol{\tau}_{4:5} = \begin{bmatrix}0\\0\end{bmatrix} = \mathbf{C}_{4:5;4:5}\boldsymbol{\alpha}_{4:5} + \mathbf{G}_{4:5} + \mathbf{D}_{4:5;4:5}\boldsymbol{\alpha}_{4:5} + \mathbf{M}_{4:5;4:5}\dot{\boldsymbol{\alpha}}_{4:5} + \mathbf{M}_{4:5,1:3}\dot{\boldsymbol{\alpha}}_{1:3} - \mathbf{K}_{2,4:5}\mathbf{z}_{2,4:5}$$

where the arguments of $\mathbf{C}$ and $\mathbf{M}$ have been dropped for notational clarity, and $(\cdot)_{i:j;k:l}$ extracts rows $i-j$, columns $k-l$ of $(\cdot)$ Solving for $\dot{\boldsymbol{\alpha}}_{4:5}$, this results in a dynamic equality constraint

$$\begin{aligned}\mathbf{M}_\alpha(\boldsymbol{\eta})\dot{\boldsymbol{\alpha}}_{4:5} = &-\mathbf{D}_\alpha\boldsymbol{\alpha}_{4:5} - \mathbf{C}_\alpha(\boldsymbol{\eta},\boldsymbol{\nu})\boldsymbol{\alpha}_{4:5}\\ &+\boldsymbol{\gamma}(\boldsymbol{\eta},\mathbf{z}_1,\mathbf{z}_2,\ddot{\mathbf{r}})\end{aligned} \tag{38}$$

where

$$\begin{aligned}\mathbf{M}_\alpha(\boldsymbol{\eta}) &= \mathbf{M}_{4:5;4:5}(\boldsymbol{\eta}),\\ &\quad \text{the lower 2x2 block of } \mathbf{M}(\boldsymbol{\eta})\\ \mathbf{C}_\alpha(\boldsymbol{\eta},\boldsymbol{\nu}) &= \mathbf{C}_{4:5;4:5}(\boldsymbol{\eta},\boldsymbol{\nu}),\\ &\quad \text{the lower 2x2 block of } \mathbf{C}(\boldsymbol{\eta},\boldsymbol{\nu})\\ \mathbf{D}_\alpha &= \mathtt{diag}\{[d,d]\} > 0\end{aligned}$$

and

$$\begin{aligned}\boldsymbol{\gamma}(\boldsymbol{\eta},\mathbf{z}_1,\mathbf{z}_2,\ddot{\mathbf{r}}) = &-\mathbf{G}_{4:5} + \mathbf{K}_{2,4:5}\mathbf{z}_{2,4:5}\\ &-\mathbf{M}_{4:5,1:3}(\ddot{\mathbf{r}} - \mathbf{K}_1\mathbf{H}\mathbf{z}_2 + \mathbf{K}_1\mathbf{K}_1\mathbf{z}_1)\end{aligned}$$

in which we have used the fact that

$$\begin{aligned}\dot{\boldsymbol{\alpha}}_{1:3} &= \ddot{\mathbf{r}} - \mathbf{K}_1\dot{\mathbf{z}}_1\\ &= \ddot{\mathbf{r}} - \mathbf{K}_1\mathbf{H}\mathbf{z}_2 + \mathbf{K}_1\mathbf{K}_1\mathbf{z}_1\end{aligned} \tag{39}$$

Also, note that the matrix $\dot{\mathbf{M}}_\alpha - 2\mathbf{C}_\alpha$ retains the skew-symetric property. The variables $\boldsymbol{\alpha}_{4:5}$ becomes a dynamic state in the controller, according to (38). In fact, (38) is a stable differential equation driven by the converging error signals $(\mathbf{z}_1,\mathbf{z}_2)$ and the bounded signal $\ddot{\mathbf{r}}$. As $\mathbf{z}_{2,4:5}(t) \to 0$, it follows that $|\boldsymbol{\alpha}_{4:5} - [\dot{\phi}_L, \dot{\theta}_L]^{\mathrm{T}}| \to 0$ as $t \to \infty$. This is stated more formally in Theorem 1.

Theorem 1 *Let the trajectory tracking problem* (20)–(21) *of a multirotor UAV be solved by applying the first three rows of the control law* (31) *to* (17)*:*

$$\begin{aligned}\mathbf{F} = &\mathbf{C}_{1:3;4:5}(\boldsymbol{\eta},\boldsymbol{\nu})\boldsymbol{\alpha}_{4:5} + \mathbf{G}_{1:3} - \mathbf{z}_1\\ &+\mathbf{M}_{1:3;1:3}(\ddot{\mathbf{r}} - \mathbf{K}_1\mathbf{H}\mathbf{z}_2 + \mathbf{K}_1\mathbf{K}_1\mathbf{z}_1)\\ &+\mathbf{M}_{1:3;4:5}\dot{\boldsymbol{\alpha}}_{4:5} - \mathbf{K}_{2,1:3}\mathbf{z}_{2,1:3} - \hat{\mathbf{w}}\end{aligned} \tag{40}$$

where $\mathbf{K}_1 > 0 \in \mathbb{R}^{3\times3}$, $\mathbf{K}_2 > 0 \in \mathbb{R}^{5\times5}$, $\mathbf{z}_1 := \mathbf{p} - \mathbf{r}$, $\mathbf{z}_2 := \boldsymbol{\nu} - \boldsymbol{\alpha}$, *and*

$$\boldsymbol{\alpha}_{1:3} = \dot{\mathbf{r}} - \mathbf{z}_1 \tag{41}$$

The smooth reference signals $\mathbf{r}$, $\dot{\mathbf{r}}$ *and* $\ddot{\mathbf{r}}$ *are provided by an external guidance system or a reference model, while* $\boldsymbol{\alpha}_{4:5}$ *are given by the dynamic system*

$$\begin{aligned}\mathbf{M}_\alpha(\boldsymbol{\eta})\dot{\boldsymbol{\alpha}}_{4:5} = &-\mathbf{D}_\alpha\boldsymbol{\alpha}_{4:5} - \mathbf{C}_\alpha(\boldsymbol{\eta},\boldsymbol{\nu})\boldsymbol{\alpha}_{4:5}\\ &+\boldsymbol{\gamma}(\boldsymbol{\eta},\mathbf{z}_1,\mathbf{z}_2,\ddot{\mathbf{r}})\end{aligned} \tag{42}$$

Then the equilibrium point $(\mathbf{z}_1,\mathbf{z}_2) = 0$ *is UGAS,* $\boldsymbol{\alpha}_{4:5} \in \mathcal{L}_\infty$ *and satisfies*

$$\lim_{t\to\infty} |\boldsymbol{\alpha}_{4:5}(t) - [\dot{\phi}_L(t), \dot{\theta}_L(t)]^{\mathrm{T}}| = 0 \tag{43}$$

Proof The closed-loop system can be expressed as

$$\Sigma_1 \begin{cases} \begin{bmatrix} \dot{\mathbf{z}}_1 \\ \dot{\mathbf{z}}_2 \end{bmatrix} = \begin{bmatrix} -\mathbf{K}_1 & \mathbf{H} \\ A_{21}(t) & A_{22}(t) \end{bmatrix} \begin{bmatrix} \mathbf{z}_1 \\ \mathbf{z}_2 \end{bmatrix} + \begin{bmatrix} 0 \\ \mathbf{M}^{-1}(\Theta(t))\mathbf{H}^{\mathrm{T}} \end{bmatrix} \tilde{\mathbf{w}} \\ \dot{\tilde{\mathbf{w}}} = \rho \mathbf{H} \mathbf{z}_2 \end{cases} \tag{44}$$

$$\Sigma_2 \begin{cases} \mathbf{M}_\alpha(\boldsymbol{\eta})\dot{\boldsymbol{\alpha}}_{4:5} = -\mathbf{D}_\alpha \boldsymbol{\alpha}_{4:5} - \mathbf{C}_\alpha(\boldsymbol{\eta}, \boldsymbol{\nu})\boldsymbol{\alpha}_{4:5} \\ \qquad\qquad + \boldsymbol{\gamma}(\boldsymbol{\eta}, \mathbf{z}_1, \mathbf{z}_2, \ddot{\mathbf{r}}) \end{cases} \tag{45}$$

From Lemma 1 we know that the origin of Σ_1 is UGAS and ULES. The unforced $\boldsymbol{\alpha}_{4:5}$ system, Σ_2 with $\boldsymbol{\gamma} = 0$, is globally exponentially stable. This can be seen from the Lyapunov function

$$V_\alpha(\boldsymbol{\alpha}_{4:5}, t) = \frac{1}{2}\boldsymbol{\alpha}_{4:5}^{\mathrm{T}} \mathbf{M}_\alpha(\boldsymbol{\eta})\boldsymbol{\alpha}_{4:5} \tag{46}$$

whos derivative along (38) is

$$\begin{aligned} \dot{V}_\alpha(\boldsymbol{\alpha}_{4:5}, t) &= \boldsymbol{\alpha}_{4:5}^{\mathrm{T}}(-\mathbf{D}_\alpha \boldsymbol{\alpha}_{4:5} + \boldsymbol{\gamma}) \\ &\leq -\frac{1}{2}\boldsymbol{\alpha}_{4:5}^{\mathrm{T}} \mathbf{D}_\alpha \boldsymbol{\alpha}_{4:5} \leq 0 \end{aligned}$$

for $||\boldsymbol{\alpha}_{4:5}||_2 > 2||\boldsymbol{\gamma}||_2/d$. Since $(\mathbf{z}_1, \mathbf{z}_2) \in \mathcal{L}_\infty$, $\mathbf{r}, \dot{\mathbf{r}}, \ddot{\mathbf{r}} \in \mathcal{L}_\infty$ and since $\boldsymbol{\eta}$ enters $\boldsymbol{\gamma}$ through the bounded functions cos and sin, we have $\boldsymbol{\gamma}(\boldsymbol{\eta}, \mathbf{z}_1, \mathbf{z}_2, \ddot{\mathbf{r}}) \in \mathcal{L}_\infty$. Thus, the $\boldsymbol{\alpha}_{4:5}$ subsystem is input-to-state stable from $\boldsymbol{\gamma}$ to $\boldsymbol{\alpha}_{4:5}$ by [16, Theorem 4.19]. Hence, $\boldsymbol{\alpha}_{4:5}$ converges to the bounded set $\{\boldsymbol{\alpha}_{4:5} : ||\boldsymbol{\alpha}_{4:5}|| \leq (2/d)||\boldsymbol{\gamma}||\}$. The limit (43) is obtained from the fact that $\mathbf{z}_{2,4:5}(t) \to 0$ as $t \to \infty$. □

Remark 1 Note that the global results presented in Theorem 1 applies to the perturbed model (17). This model is valid as long as the wire is taut, and we stay away from the representation singularity at $\theta_L = \pi/2$. At this point, the model is perturbed by the infinitesimal constant ε, which in practice will have negligible impact on the results.

Remark 2 Also, note that the load angles ϕ_L and θ_L are not included in the coordinate change (20)–(21), but their derivatives are. The angles acts as external inputs to the system dynamics through the saturating geometric functions cos and sin, and are thus treated as bounded inputs in the analysis. See Figure 3.

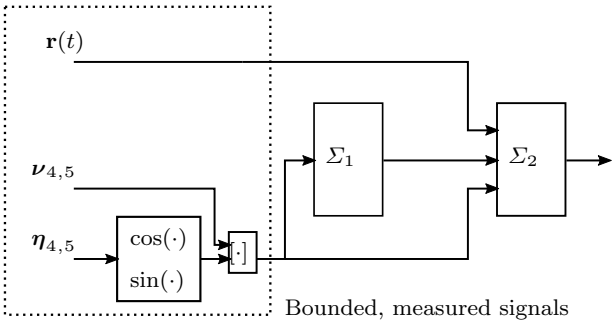

Fig. 3 Structure illustrating the proof. By Theorem 1, the feedback law (40) renders the origin of $[\mathbf{z}_1, \mathbf{z}_2]$ globally asymptotically stable. The signal $\boldsymbol{\alpha}_{4,5}$, needed by (40), is shown to be bounded. The load angles act on both subsystems through the saturating trigonometric geometric functions cos(·) and sin(·), and $\boldsymbol{\nu}_{4,5}$ is bounded by (43).

4.4 Implementational Aspects

When implementing backstepping controllers, it is often advantageous to re-write the final control output in the original UAV coordinates to facilitate easier tuning of the various gains. Indeed, by re-writing the controller equation (40), and define the error signal $\tilde{\mathbf{p}} := \mathbf{p} - \mathbf{r}$, the PID-like structure can be recovered:

$$\begin{aligned} \mathbf{F} =& \boldsymbol{\beta}(\cdot) + \mathbf{G}(\boldsymbol{\eta}) + (m_L + m_c)\ddot{\mathbf{r}} \\ & - \mathbf{K}_d\dot{\tilde{\mathbf{p}}} - \mathbf{K}_p\tilde{\mathbf{p}} - \mathbf{K}_i \int_0^t \tilde{\mathbf{p}}\, \mathrm{d}\tau \end{aligned} \tag{47}$$

where we recognize the gravity compensation, reference acceleration feed forward, the proportional, derivative and integral feedback terms. In addition, the stabilizing load compensator $\beta(\cdot)$ which is a function of $(\boldsymbol{\eta}, \boldsymbol{\nu}, \mathbf{r}, \dot{\mathbf{r}}, \ddot{\mathbf{r}}, \boldsymbol{\alpha}_{4,5})$, acts to cancel the effects of the suspended load. It is given by

$$\boldsymbol{\beta} = \mathbf{C}_{1:3,4:5}(\boldsymbol{\eta}, \boldsymbol{\nu})\boldsymbol{\alpha}_{4:5} + \mathbf{M}_{1:3,4:5}\dot{\boldsymbol{\alpha}}_{4:5} \tag{48}$$

and where $\boldsymbol{\alpha}_{4:5}$ is driven by the dynamic constraint

$$\begin{aligned} \mathbf{M}_\alpha\dot{\boldsymbol{\alpha}}_{4:5} =& -(\mathbf{D}_\alpha + \mathbf{C}_\alpha(\boldsymbol{\eta}, \boldsymbol{\nu}) + \mathbf{K}_{2,4:5})\boldsymbol{\alpha}_{4:5} \\ & - \mathbf{G}_{4:5} + \mathbf{K}_{2,4:5}\dot{\boldsymbol{\Theta}} - \mathbf{M}_{4:5,1:3}(\boldsymbol{\eta})(\ddot{\mathbf{r}} - \mathbf{K}_1\dot{\tilde{\mathbf{p}}}) \end{aligned} \tag{49}$$

and the gains are given by

$$\mathbf{K}_p = \mathbf{I} + \mathbf{K}_{2,1:3}\mathbf{K}_1 + \rho\mathbf{I} \tag{50}$$

$$\mathbf{K}_d = (m_L + m_c)\mathbf{K}_1 + \mathbf{K}_{2,1:3} \tag{51}$$

$$\mathbf{K}_i = \rho\mathbf{K}_1 \tag{52}$$

As the dominating elements of (47) are the proportional and derivative terms, (50)–(52) allows the use of tools like pole-placement for linear systems to be used when tuning the final controller.

4.5 Generating Reference Signals

The controller presented above requires a smooth $\mathcal{C}^3$ trajectory. Given a sequence of waypoints given by the operator, the trajectory can be generated by feeding the waypoints through a reference model of sufficient order. Consider a fourth order low-pass filter:

$$\mathbf{x}^{(4)}+4\zeta\omega_0\mathbf{x}^{(3)}+(2+4\zeta^2)\omega_0^2\ddot{\mathbf{x}}+4\zeta\omega_0^3+\omega_0^4\mathbf{x}=\omega_0^4\mathbf{x}_d \quad (53)$$

where $\mathbf{x} \in \mathbb{R}^3$ is the reference signal, $\mathbf{x}_d \in \mathbb{R}^3$ is the current desired position (waypoint), and $\zeta, \omega \in \mathbb{R}$ are tuning parameters. Consider only the first dimension of $\mathbf{x}$, a reference position of $\mathbf{x}_{d,1} = 20$ would give the trajectory illustrated by the dashed lines in Figure 4. However, this is not a feasible trajectory for the UAV as the UAV encompasses certain dynamic constraints, like maximum acceleration and jerk, that is not taken into account. Further, the operator would typically like to set a prescribed velocity for the maneuver. Thus, in this work, we re-arrange (53) as a set of cascaded controllers, and impose saturations on each level of the cascade to facilitate the constraints of the UAV. That is;

$$\mathbf{x}^{(4)} = \mathbf{u} \quad (54)$$

$$\tau_1 = \text{sat}(\text{k}_1(\mathbf{x}^{\text{d}} - \mathbf{x}), \text{v}_{\max}) \quad (55)$$

$$\tau_2 = \text{sat}(\text{k}_2(\tau_1 - \mathbf{x}^{(1)}), \text{a}_{\max}) \quad (56)$$

$$\tau_3 = \text{sat}(\text{k}_3(\tau_2 - \mathbf{x}^{(2)}), \text{j}_{\max}) \quad (57)$$

$$\mathbf{u} = k_4(\tau_3 - \mathbf{x}^{(3)}) \quad (58)$$

The parameters $k_i, i \in \{1, \ldots, 4\}$ are found by inspection of (53) as

$$k_4 = 4\zeta\omega_0 \qquad k_3 = \frac{(2+4\zeta^2)\omega_0^2}{k_4}$$

$$k_2 = \frac{4\zeta\omega_0^3}{k_4 k_3} \qquad k_1 = \frac{\omega_0^4}{k_4 k_3 k_2}$$

We are now able to impose constraints on the motion by setting v_{max}, a_{max} and j_{max} appropriately. Consider again the first dimension, with the aforementioned constraints set 3 m/s, 1.5 ms^2 and 3 m/s^3 respectively, the resulting trajectory can be seen by the solid lines in Figure 4. Clearly, we see that the response is slower, but complies the constraints. This reference-model is now used to generate feasible, smooth $\mathcal{C}^3$ trajectories for the controller.

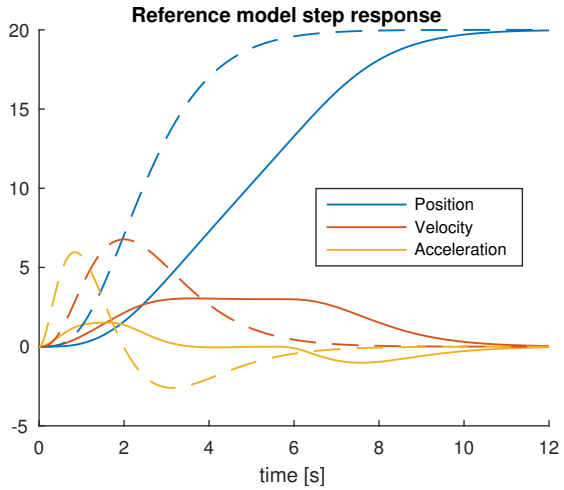

Fig. 4 Step response of the reference model. The dashed lines corresponds to a regular low-pass filter, while the solid lines represents the response of the augmented reference model, which complies with the dynamical constraints of the UAV.

5 Results Tracking Controller

This section presents the results of the performance of the controller structure derived above. The results are verified in a numerical simulation and in a UAV experiment, with a step-like trajectory.

The simulation parameters are set to match that of the experimental platform, and are summarized in Table 1. The simulation is conducted in MATLAB, using the model presented Section 3. Integration is performed using *Runge-Kutta-4* at 20 Hz.

Table 1 UAV Data

UAV Mass	2.5	kg
Payload Mass	250	g
Suspension Length	4.2	m
Speed Setpoint	4	m/s
Maximum Acceleration	7	m/s^2

5.1 UAV Platform

The UAV platform is a hexacopter, equipped with the *Pixhawk* [24] autopilot system running Ardupilot [4] software. This autopilot handles sensor fusion from its internal IMU and GNSS systems, as well as low level attitude control. It receives attitude and thrust setpoints from an on-board Linux computer, a Beaglebone Black, which contains the custom controller described in this work. The Beaglebone is a 1 GHz single-board ARM computer, running the LSTS toolchain [23]. This toolchain consists of a Linux distribution (Glued), a ground station segment (Neptus) and a vehicle software

stack (DUNE). All implementations for the experimental validation is implemented in DUNE using C++. See Figure 1.

The displacement angles of the suspended load is measured by two magnetic encoders, the MTS360 [22]. At the day of testing, the wind conditions were moderate (about 3-4 m/s), with gusts up to 5-6 m/s.

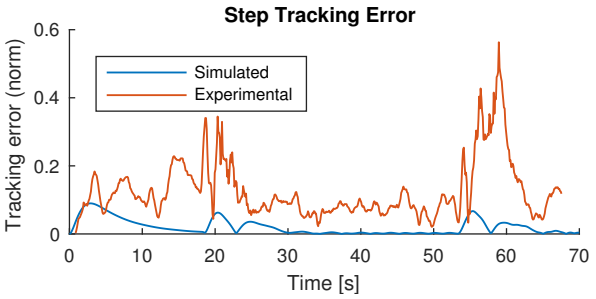

Fig. 6 Tracking error when running the controller with a step-input. The desired position is 20 m away from the initial position.

5.2 Step-like Trajectory

In this validation case, the desired trajectory is a 20 m displacement in the horizontal plane. In both the simulation and experiment, the controller needs to compensate for an unknown wind disturbance. Figure 5 illustrates the distance traveled during the test, while Figure 6 shows the tracking-error of the controller in both the experimental and simulated setting. As can be seen, the controller tracks the desired trajectory satisfactorily, where in the experimental case the average tracking error is 12.5 cm. There are peaks approaching 60 cm however, which corresponds to the time when the UAV stops at the final position. The wind disturbance estimation magnitude is illustrated in Figure 7, which we see for the simulation case that the controller approaches the correct steady-state value. In the experimental case, we see fluctuations, which is induced by wind gusts and the elevated tracking error during aggressive parts of the maneuver. As Figure 8 shows, there is naturally a substantial load deflection during acceleration. Especially for the simulated case, we see that the load continues to oscillate when the UAV reaches hover state. Due to un-modeled effects the response in the experiments are of lower amplitude, but the oscillations are clearly visible. In the next section, we discuss how to design the reference trajectory as to minimize the suspended load swing.

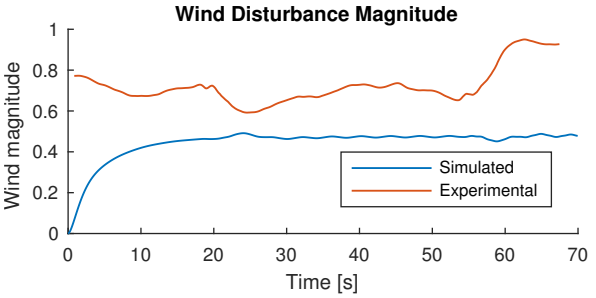

Fig. 7 Magnitude of the wind disturbance estimation during the step test case. In the simulated case, the magnitude trends towards the unknown constant bias. For the experimental case, the wind estimate fluctuates significantly more due to the shifting wind conditions during the experiment.

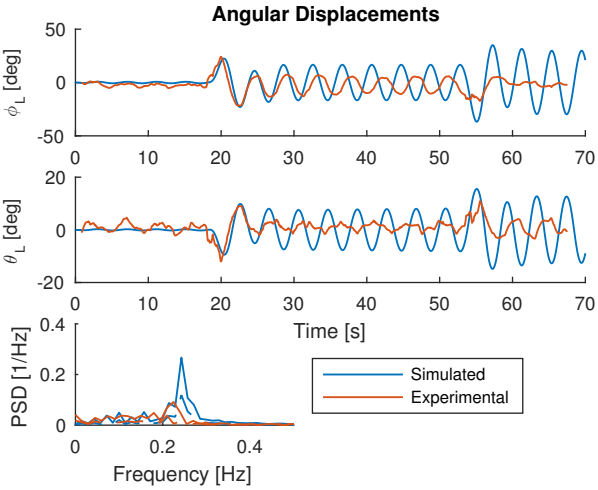

Fig. 8 Angles of the suspended load running the step type trajectory. The lower-left plot illustrates the *Power Spectral Density* over the frequency range of pendulum swing.

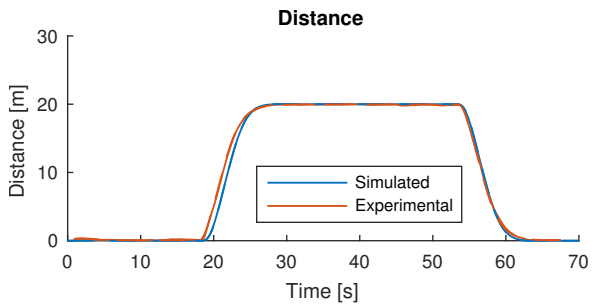

Fig. 5 The distance trajectory during the step test case.

6 Damping of suspended load oscillations

To safely transport a suspended payload with an UAV, the swing motion of the payload should be kept small. This type of problem has a vast history in the literature,

especially for usage on overhead cranes [1], but also on various flying vehicles. The use of Input Shaping is one of the most practical open-loop control strategies for these problems, and has been widely used [25]. Its main concept is that by giving the UAV two consecutive step inputs, the oscillatory response between the two cancels each other out, and resulting in a oscillation free maneuver. However, it as it is open loop, it is sensitive to modeling uncertainties.

The impulse response of the simplest input-shaping filter $\mathcal{I}$ can be seen in Figure 9 as two pulses at times $t_1 = 0$ and t_2, of amplitudes $A1$ and $A2$, respectively. Given the damped natural frequency ω_d and damping ratio ζ, the filter coefficients can be calculated as [7]:

$$t_1 = 0 \qquad t_2 = \frac{\pi}{\omega_d} \tag{59}$$

$$A_1 = \frac{1}{1+K} \qquad A_2 = \frac{K}{1+K} \tag{60}$$

$$K = \exp\left(\frac{-\zeta\pi}{\sqrt{1-\zeta^2}}\right) \tag{61}$$

For a suspended load, the natural frequency of oscillations is given by $\omega_n = \sqrt{g/L}$. Given a reference trajectory $\bar{\boldsymbol{\xi}}(t) := [\mathbf{r}(t), \dot{\mathbf{r}}(t), \ddot{\mathbf{r}}(t)]$, the resulting desired trajectory is obtained by the convolution of the shape filter:

$$\boldsymbol{\xi}_I = \bar{\boldsymbol{\xi}} * \mathcal{I} \tag{62}$$

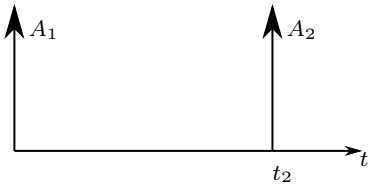

Fig. 9 Impulse response of the input shape filter $\mathcal{I}$, tuned after the frequency response of the pendulum-motion of the suspended load.

In Figure 10, an illustrative example shows the effect of shaping the reference trajectory in this matter. As can be seen, the response is lagging behind the original trajectory, but the residual swings are greatly reduced.

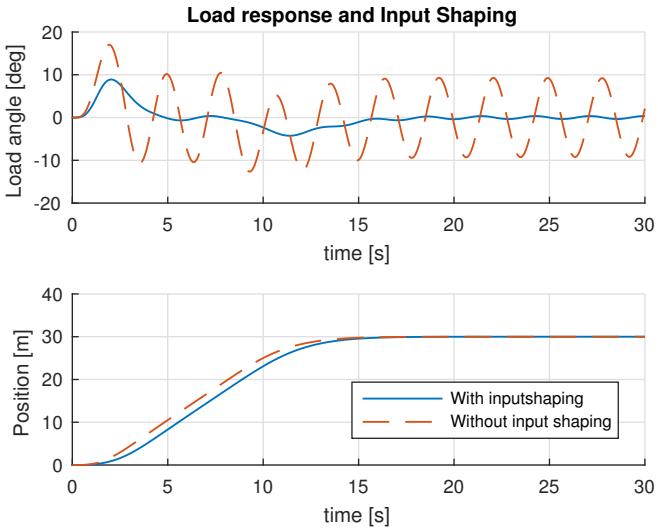

Fig. 10 Illustrative example of the effects of open-loop trajectory generation using input shaping.

Another technique would be to use feedback from a measured load angle as means to damp the oscillatory motion of the suspended load. In this article, we are utilizing an approach called *Delayed feedback control* [8] to actively damp the swing motion. As illustrated in [8], it is capable of damping out the residual swing during hover or steady transit. The technique is based on adding a feedback-component from the measured deflection angle on the reference signal sent to the controller. Consider the one dimensional auxiliary reference signal

$$x_r(t) = G_d L \sin\left(\theta_L(t - \tau_d)\right) \tag{63}$$

where G_d and τ_d are design-parameters, designed as to dampen out the swing load. As can be seen, the added reference signal purposefully induces a *delay* in the feedback loop to achieve the damping. While the readers are referred to [8] for details on the design procedure, for the multirotor UAV we sutilize the following parameters:

$$G_d = 0.325, \;\; \tau_d = 0.325\frac{2\pi}{\omega_d} \tag{64}$$

To utilize the delayed feedback controller, consider the y-axis equivalent of (63), $y_r(t) = -G_d L \sin\left(\phi_L(t - \tau_d)\right)$, and aggregate the first and second derivatives to

$$\boldsymbol{\xi}_D = \begin{bmatrix} x_r & y_r & 0 & \dot{x}_r & \dot{y}_r & 0 & \ddot{x}_r & \ddot{y}_r & 0 \end{bmatrix} \tag{65}$$

The structure of the total feed forward plus delayed feedback reference generator can then be seen in Figure 11. This is a similar structure as presented in [8].

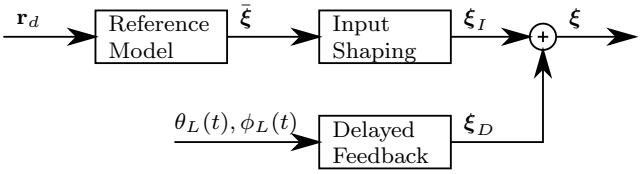

Fig. 11 Traditional overall structure for combining feedforward input shaping with delayed feedback for trajectory generation.

An example showcasing the delayed feedback controller (compared with the input-shaping feed forward) is seen in Figure 12. As can be seen, the feedback controller is removing all of the residual oscillations. However, during start and stop, it produces unnecessary large oscillations in the load angle and resulting UAV velocity, as can be seen by the peak in Figure 12.

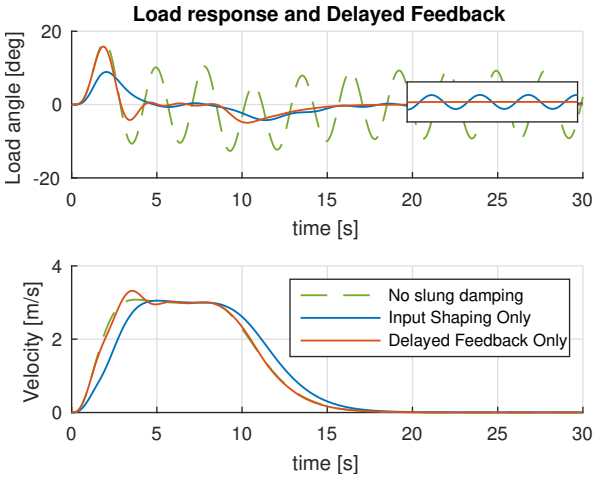

Fig. 12 The delayed feedback controller cancels out the residual swing, but produces unwanted peaks in reference velocity.

As can be deducted from this, the feedforward shaping filter does a good job during the transients, but are susceptible to modeling errors and residual swings. The feedback term on the other hand, is overreacting during the transients but does a good job at canceling the lingering oscillations. The direct combination of the two, as illustrated in Figure 11, does a fairly decent job at maintaining the benefits of both terms. But, there is still some unwanted velocity peaks and overreacting from the feedback structure during the transients. This is kind of natural, as the job of the feedforward is to allow an initial swing, but then cancel it by the second impulse. By having the feedback term active all of the time, it renders parts of the feedforward terms more inaccurate. Thus, we would like to smoothly disable the feedback term during the transients.

By examining the full dynamic model in (12), it can be observed that the UAV only influence the suspended load motion through acceleration. Thus, we propose to introduce a smooth gain-scheduling approach for the delayed feedback, using the recent history of reference acceleration as input. Specifically, let

$$\mathbf{a}_k := \begin{bmatrix} a_k & a_{k-1} & a_{k-1} & \cdots & a_{k-N} \end{bmatrix} \tag{66}$$

where $a_k := ||\ddot{r}(t_k)|| \in \mathbb{R}$ is the total reference acceleration at time t_k, for some constant number of samples N. Further, let p_k be the *percentage of values in* $\mathbf{a}_k$ *less than a acceleration threshold* a_t. That is;

$$p_k = \frac{1}{N} \sum_{i=0}^{N} \begin{cases} 1 & \text{if } a_{k-i} < a_t \\ 0 & \text{else} \end{cases} \tag{67}$$

Let p_k be the input to a sigmoid-type function. We utilize the *logistic function*

$$S(p_k) := \frac{1}{1 + e^{-k(p_k - p_c)}} \tag{68}$$

where $k, p_c \in \mathbb{R}$ can be tuned to vary the shape of $S(p_k)$. Figure 13 shows such a sigmoid function for $k = 30, p_c = 0.7$. Subsequently, we get the structure depicted in Figure 14 where we can see that the sigmoid gain block $S(p_k)$ adjusts the contribution from the delayed feedback based on the reference acceleration of the unperturbed trajectory $\boldsymbol{\xi}_I$. The effect of this scheme can be seen in Figure 15, where we can see that the residual oscillations are cancelled out and the UAV avoids the unnecessary velocity peaks.

The complete interconnected slung-load controller is now depicted in Figure 16.

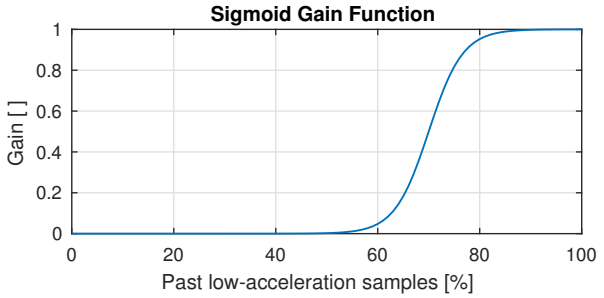

Fig. 13 Illustration of the sigmoid function. By looking at the history of reference accelerations, the gain is increased when we are at steady state for maneuvering.

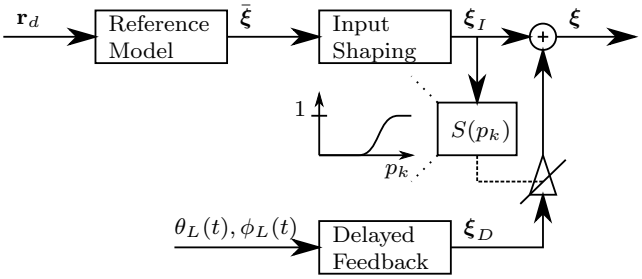

Fig. 14 Proposed structure for combining the feed forward input shaper with delayed feedback. Using the current and recent reference accelerations from $\boldsymbol{\xi}_I$, the block $S(p_k)$ smoothly activates the feedback path only on constant velocity part of a maneuver (including hover).

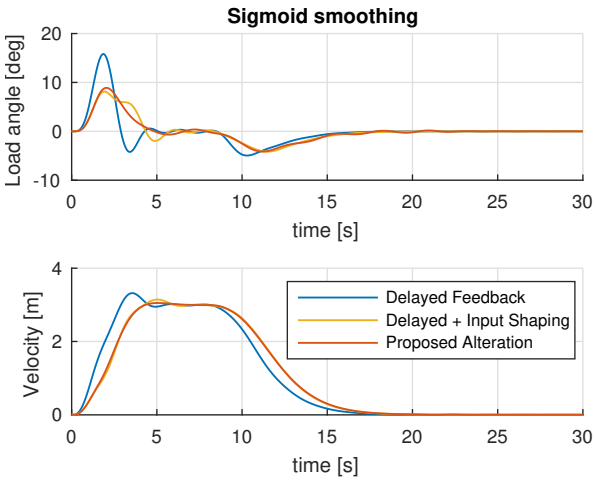

Fig. 15 The result when using the proposed sigmoid gain function

this is a viable tradeoff when taking the pronounced benefit of the reduced load motion into account.

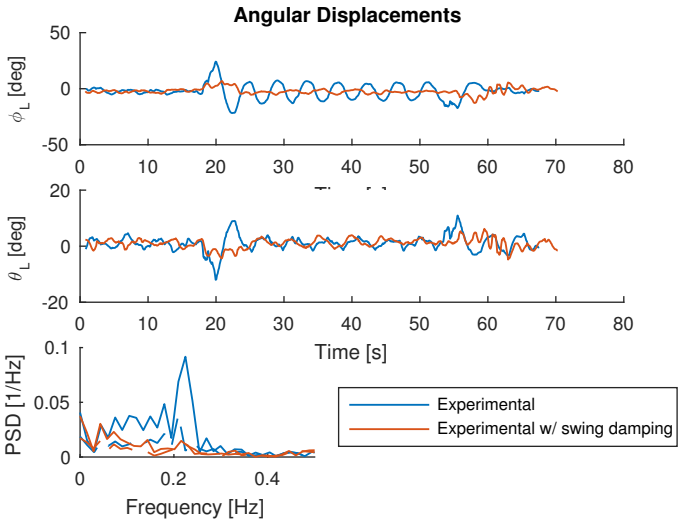

Fig. 17 Angular response during the experiment, running a step-like input. With the swing damping enabled, the oscillations are of lower amplitude and are damped faster. The lower-left plot shows the *power spectral density* of the angular signal.

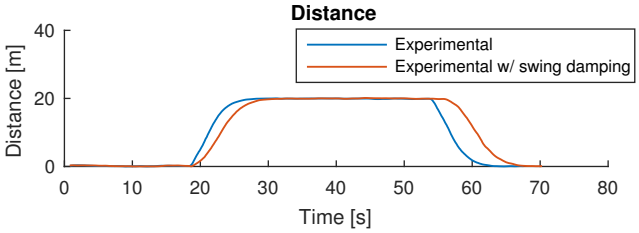

Fig. 18 Distance travelled during the step-like input.

7 Results: Tracking Controller with Swing Damping

7.1 Step-like Trajectory

To verify the performance of the tracking controller with the proposed swing-damping technique, we first do the same step-maneuver as in Section 5. Figure 17 shows the experimental results with and without swing damping. Clearly, there is substantially less angular motion of the suspended load with the swing damping enabled. This is also visible from the power spectral density in the lower-left of Figure 17, where we see that the natural frequencies are now less dominant than secondary oscillatory effects from the UAV motion. Figure 18 shows the lag-effect of the input shaper, where the second experiment lags a bit behind the first without the swing damping enabled. For most applications,

7.2 Figure-8-like Trajectory

Further, we tested the performance for a more complicated figure-8 like trajectory which we compare with a similar trajectory without any swing damping. For both cases, the trajectory includes a 20 second hover state at the beginning the maneuver. The resulting North-East path can be seen in Figure 19. From Figure 20, it can be seen that the tracking error is of the same magnitude as without the swing damping, but looking at the angular displacements in Figure 22, the difference is more striking. The suggested structure is able to greatly reduce the angular displacements. The wind disturbance estimation can be seen in Figure 21, which in both cases varies over the course of the experiment. This is partly due to gusts, but it is also reacting to the somewhat higher average tracking error during the end of the maneuver due to aggressive turning. Also, note

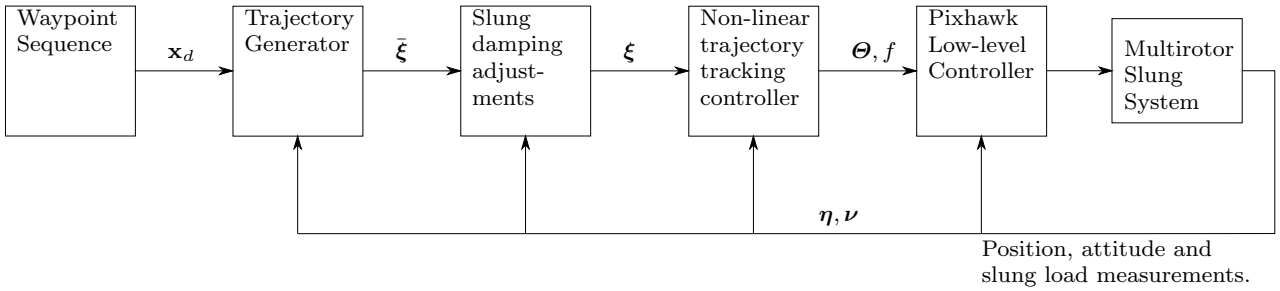

Fig. 16 The complete controller structure, illustrating the signals flowing through the various main components. The physical system, including state estimation and measurement of the slung load deflection angles, is represented in the block *Multirotor Slung System*.

that due to the sequence of experiments conducted, the case where the swing damping was enabled had a soft-start of the bias estimation. However, due to the initial hover state, the controller have a reasonable time to reach estimation steady state before the maneuver commences which can be observed in the plot.

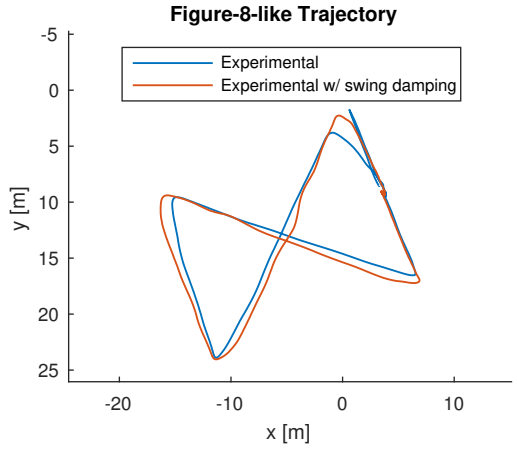

Fig. 19 Trajectories during the figure-8-like maneuver. The discrepancies is due to the altered desired trajectory from the swing-damping.

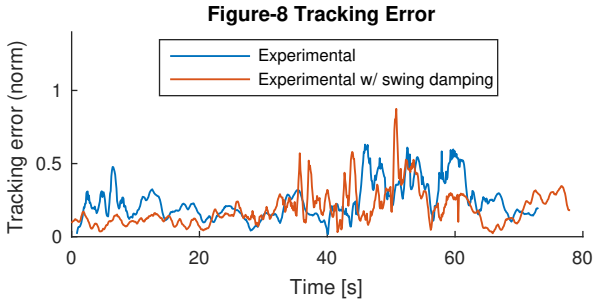

Fig. 20 Tracking errors along the desired trajectory.

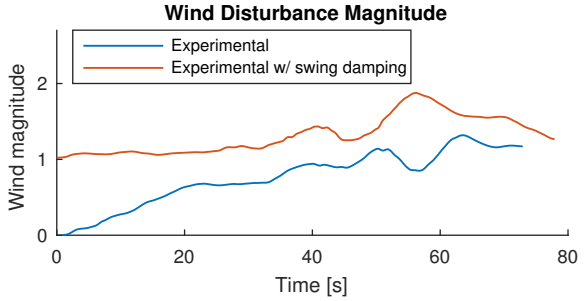

Fig. 21 The estimated wind disturbance magnitude during the figure-8-like maneuver.

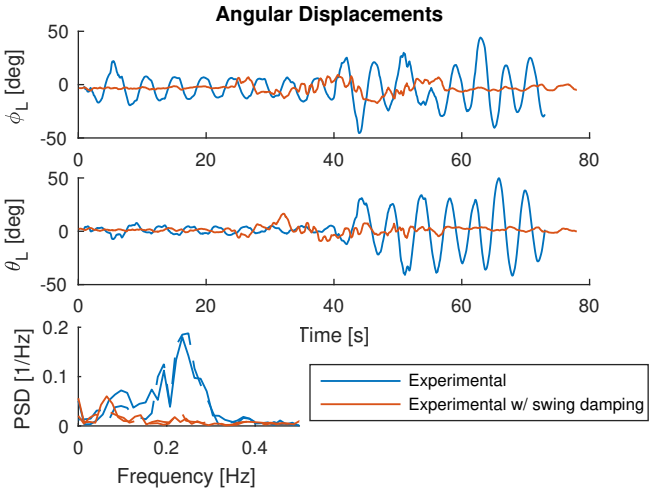

Fig. 22 Suspended load displacement angles during the figure-8-like maneuver. The peak of the *power-spectral-density* graph on the lower left corresponds to the natural oscillation frequency of the undamped load.

8 Final Discussion and Conclusion

In this paper, we have studied a multirotor UAV carrying a suspended load. By utilizing Kane's equation, a non-linear model of the interconnected dynamics was derived. Further, a trajectory tracking controller based on the backstepping technique was designed. Due to the presence of wind disturbances, the controller includes a

wind bias compensator in the form of an added integral effect. The origin of the tracking error was proven UGAS and ULES.

To dampen the deflection angles of the oscillating suspended load, we considered an open-loop and a feedback type trajectory generation approach from the literature. We proposed a new method to combine these two approaches using a gain-scheduling procedure based on recent acceleration reference points.

The controller and proposed swing damping methodology was verified using both numerical simulation and experimental data from a in-house built low-cost UAV platform. All experiments were conducted outside, and implementation was done in a application framework applicable for continuous use and research.

Acknowledgements This work was partially supported by the Research Council of Norway through its Centers of Excellence funding scheme, grant number 223254 (Centre for Autonomous Marine Operations and Systems).

A Desired Force to Attitude

This section outlines how one translates a desired force $\mathbf{F}_d$ to desired Euler angles ϕ_d, θ_d and ψ_d. It turns out, the desired yaw angle ψ_d can be set independently of the desired force. The body-oriented forces $\mathbf{F}^{\bar{b}}$ obtained by a principal rotation of $\mathbf{F}$ around the z-axis with the current yaw ψ relates to the roll- and pitch angles as follows

$$F_x^{\bar{b}} = -k_f f \cos\phi \sin\theta \tag{69}$$

$$F_y^{\bar{b}} = \quad k_f f \sin\phi \tag{70}$$

$$F_z^{\bar{b}} = -k_f f \cos\phi \cos\theta \tag{71}$$

where $f \in [0..1]$, and $k_f \in \mathbb{R}$ is a coefficient of the thrust configuration typically s.t. at $f = 0.5$ the vehicle is at hover. This equation set can be solved by first solving (71) for f using the current values for ψ and θ. Then, solve (69)–(70) for ϕ and θ, giving the desired values.

To further simplify; if one assumes low vertical accelerations, the desired roll- and pitch angles can be found by

$$\theta_d = \arctan \frac{-F_x^{\bar{b}}}{mg} \tag{72}$$

$$\phi_d = \arctan \frac{F_y^{\bar{b}} \cos\theta_d}{mg} \tag{73}$$

References

1. Abdel-Rahman, E., Nayfeh, A., Masoud, Z.: Dynamics and control of cranes: A review. Journal of Vibration and Control **9**(7), 863–908 (2003). DOI 10.1177/107754603031852
2. Amazon: Amazon.com (2016). URL http://www.amazon.com/b?node=8037720011
3. Angeli, D., Sontag, E.D.: Forward completeness, unboundedness observability, and their Lyapunov characterizations. Systems & Control Letters **38**(4), 209–217 (1999). DOI 10.1016/S0167-6911(99)00055-9
4. Ardupilot.com: Ardupilot - Open source autopilot (2016). URL http://ardupilot.com
5. Bernard, M., Kondak, K.: Generic slung load transportation system using small size helicopters. 2009 IEEE International Conference on Robotics and Automation pp. 3258–3264 (2009). DOI 10.1109/ROBOT.2009.5152382
6. Bernard, M., Kondak, K., Maza, I., Ollero, A.: Autonomous transportation and deployment with aerial robots for search and rescue missions. Journal of Field Robotics **28**(6), 914–931 (2011). DOI 10.1002/rob
7. Bisgaard, M., la Cour-Harbo, A., Bendtsen, J.: Input Shaping for Helicopter Slung Load Swing Reduction. In: AIAA Guidance, Navigation and Control Conference and Exhibit. Honolulu, Hawai (2008)
8. Bisgaard, M., Cour-harbo, A., Bendtsen, J.D.: Swing Damping for Helicopter Slung Load Systems using Delayed Feedback. Proceedings of AIAA Conference on Guidance, Navigation, and Control pp. 1–11 (2009)
9. Cicolani, L., Kanning, G.: Equations of motion of slung-load systems, including multilift systems. NASA, Office of Management Scientific and Technical Information Program **Technical**(3280) (1992)
10. Egeland, O., Gravdahl, J.T.: Modeling and Simulation for automatic control. Marine Cybernetics (2002)
11. Fossen, T., Breivik, M., Skjetne, R.: Line-of-Sight Path Following of Underactuated Marine Craft. In: Proc. of the IFAC MCMC'03, pp. 1–6. IFAC MCMC'03, Girona, Spain (2003)
12. Fossen, T.I.: Marine Craft Hydrodynamics and Motion Control. Wiley (2011)
13. Fossen, T.I., Loría, A., Teel, A.: Theorem for UGAS and ULES of (passive) nonautonomous systems: robust control of mechanical systems and ships. International Journal of Robust and Nonlinear Control **11**(2), 95–108 (2001). DOI 10.1002/rnc.551
14. Goodarzi, F.A., Lee, D., Lee, T.: Geometric Stabilization of Quadrotor UAV with a Payload Connected by Flexible Cable. In: American Control Conference (ACC), pp. 4925–4930. IEEE (2014)
15. Guerrero, M.E., Mercado, D.A., Lozano, R., Garc, C.D.: IDA-PBC Methodology for a Quadrotor UAV Transporting a Cable-Suspended Payload. In: Unmanned Aircraft Systems (ICUAS), 2015 International Conference on, pp. 470 – 476. IEEE, Denver, CO (2015). DOI 10.1109/ICUAS.2015.7152325
16. Khalil, H.K.: Nonlinear Systems, 3rd edn. Prenctice Hall (2002)
17. Klausen, K., Fossen, T.I., Johansen, T.A.: Nonlinear Control of a Multirotor UAV with Suspended Load. In: Unmanned Aircraft Systems (ICUAS), 2015 International Conference on, pp. 176 – 184. IEEE, Denver, CO (2015). DOI 10.1109/ICUAS.2015.7152289
18. Krstic, M., Kanellakopoulos, I., Kokotovic, P.: Nonlinear and adaptive control design. John Willey, New York (1995)
19. Mahony, R., Kumar, V., Corke, P.: Modeling, Estimation, and Control of Quadrotor. IEEE Robotics and Automation magazine **19**(3), 20–32 (2012). DOI 10.1109/MRA.2012.2206474
20. Palunko, I., Cruz, P., Fierro, R.: Agile Load Transportation - Safe and Efficient Load Manipulation with Aerial Robots. IEEE Robotics & Automation Magazine (September 2012), 69–79 (2012)

21. Palunko, I., Fierro, R., Cruz, P.: Trajectory generation for swing-free maneuvers of a quadrotor with suspended payload: A dynamic programming approach. 2012 IEEE International Conference on Robotics and Automation pp. 2691–2697 (2012). DOI 10.1109/ICRA.2012.6225213
22. Piher.net: MTS-360 (2016). URL http://www.piher.net/
23. Pinto, J., Dias, P.S., Martins, R., Fortuna, J., Marques, E., Sousa, J.: The LSTS toolchain for networked vehicle systems. OCEANS 2013 MTS/IEEE Bergen: The Challenges of the Northern Dimension (2013). DOI 10.1109/OCEANS-Bergen.2013.6608148
24. Pixhawk.ethz.ch: PX4 Pixhawk (2016). URL https://pixhawk.ethz.ch/
25. Singh, T., Singhose, W.: Input Shaping / Time Delay Control of Maneuvering Flexible Structures. In: American Control Conference, 2002. Proceedings of the 2002, pp. 1717 – 1731 (3). NY, USA (2002)